# NEW DISCOVERIES IN THE TERNARY TRANSITION METAL PNICTIDE CLASS OF ZINTL PHASES

by

Dereck Keith Wilson

A thesis submitted to the Faculty of the University of Delaware in partial fulfillment of the requirements for the degree of Master of Science in Chemistry and Biochemistry

Spring 2010

**NEW DISCOVERIES IN THE TERNARY TRANSITION METAL PNICTIDE CLASS OF ZINTL PHASES**

by

Dereck Keith Wilson

Approved: _____
Svilen Bobev, Ph.D.
Professor in charge of thesis on behalf of the Advisory Committee

Approved: _____
Klaus H. Theopold, Ph.D.
Chair of the Department of Chemistry and Biochemistry

Approved: _____
George H. Watson, Ph.D.
Dean of the College of Arts and Sciences

Approved: _____
Debra Hess Norris, M.S.
Vice Provost for Graduate and Professional Education

## ACKNOWLEDGMENTS

I would like to acknowledge my advisor, Dr. Svilen Bobev, as well as the entire Bobev research group. Dr. Paul Tobash and Dr. Shengqing Xia for their assistance in the synthesis and unit cell calculations for some of the title compounds.

I would also like to acknowledge Dr. Chao Ni and Frank Kriss of the W.M. Keck Electron Microscopy Facility for their instruction on the use of the TEM and SEM.

## TABLE OF CONTENTS

## LIST OF TABLES

## LIST OF FIGURES

## ABSTRACT

The crystal structures of the new intermetallic compounds $Eu_2ZnPn_2$ (Pn = Sb, Bi) and $Sr_2ZnPn_2$ (Pn = Sb, Bi) are reported. They have been synthesized from their corresponding elements through high-temperature reactions using the flux-growth method. The structures for $Eu_2ZnPn_2$ (Pn = Sb, Bi) and $Sr_2ZnPn_2$ (Pn = Sb, Bi) have been established by single-crystal X-ray diffraction. In those cases, the X-ray patterns can be successfully indexed based on a hexagonal cell with unit cell parameters in the range $a$=4.6-4.7 Å and $c$=8.2-8.5 Å. Structure solutions in the space group $P6_3/mmc$ suggest the defect ZrBeSi type (Pearson's symbol hP6; 3 unique positions) as the likely model; however, subsequent refinements indicate nearly 50% occupancy on the Zn site. Based off the evidence that I will present in the following paper, I believe it is plausible that the crystal structures of the reported compounds have a long-range order of zinc-vacancies. These systematic vacancies further suggest the compounds may have thermoelectric properties. Evidence for such was sought using powder X-ray diffraction, single crystal X-ray diffraction, electron diffraction, X-ray dispersive spectroscopy, and magnetic susceptibility measurements.

# Chapter 1

## INTRODUCTION

Thermoelectric devices provide significant opportunities for using solid-state materials to produce electrical power from waste heat. Waste heat can be recovered from energy-intensive industrial processes, vehicle exhaust, as well as solar applications. By definition, they are static thermal-to-electric energy conversion devices with a high degree of redundancy, no electromagnetic interferences, and no vibrations.[1] Thermoelectric power sources have proven their reliability and longevity in applications where unattended operation in remote locations is required.[2-4] This concept is extremely intriguing in today's scientific and engineering communities due to the push to discover and create more efficient and environmentally friendly power sources. Many scientists in the field of solid-state chemistry are working to find new thermoelectric materials. One general idea is that the material has "Phonon-Glass, Electron-Crystal" properties.

The idea that a material exhibits "Phonon-Glass, Electron-Crystal" properties, or PGEC is nothing new.[5,6] Typically, the PGEC concept is associated with materials that are potential sources of thermoelectric power generation. G.A. Slack first expressed this concept almost 30 years ago, and it continues to be used today. The concept basically states that PGEC materials possess electronic properties paralleling

those of good semiconductor single crystals, but retain a thermal conductivity typical of an amorphous material.[5] The semiconductor single crystal region of the material would provide a high mobility electronic structure, while interwoven with a phonon inhibiting structure.[6] The phonon inhibiting region could arise from disorder within the structure or added dopants; providing neither interferes with the electron-crystal region. Recent experiments have shown that complex Zintl phases (the product of a reaction between an alkali or alkaline earth metal and a post transition metal) make ideal candidates for thermoelectric materials because their PGEC properties can be engineered with an understanding of the Zintl chemistry.[7]

Eduard Zintl defined the Zintl border as the line between groups 13 and 14 which supposedly divides the post-transition elements capable of forming Zintl phases (to the right) from those that form truly intermetallic phases.[8] Zintl phases are compounds formed by the synthesis of an alkali or alkaline earth metal (Groups 1 and 2) and a post transition metal (usually from Groups 14 and 15). The metals from Groups 1 and 2 are electropositive cations which donate their electrons to the post transition metals, the electronegative anions. Generally, the main structural features of Zintl phases is understood by assuming that the more electropositive components (alkali, alkaline-earth metals, etc) transfer their valence electrons to the post-transition elements which then achieve closed-shell  states, either as isolated entities or polyatomic structures.[9] This is further simplified when stated as the electropositive cations form ionic bonds with the electronegative anionic arrangements.

Unfortunately, the properties of Zintl phases are not as simple as their general rule of bonding. While many Zintl phases exhibit the predicted properties of

semiconductors or insulators, many others exhibit metallic behavior.[9] The unique combination of metal-metal interactions that are not characteristic of typical covalent or ionic solids ends up defining the crystal chemistry of these compounds.[10] Zintl phases have diverse and complicated structures that quite often produce an assortment of unpredictable physical properties that has lead to the extension of this classification to include some electropositive lanthanides (europium and ytterbium) and transition metal elements.[11-17] Though a cationic element donates an electron to an anionic element in order to satisfy valence, Zintl phases are often explained with ionic and covalent contributions to the overall bonding of the structure.[7] In Zintl phases, it is the Zintl anions that provide the "electron-crystal" electronic structure through covalently bonded polyanions. The polyanion bonding can provide high mobility to electrons because of the existence of nonbonding or partially bonding states that fill the gap region and make the compound metallic.[7] The cations within Zintl phases provide regions to control electron concentration and lower lattice thermal conductivity by disrupting phonon transport. Zintl phases offer great potential for thermoelectric applications because their compounds model the PGEC concept.

Thermoelectric materials are judged by measuring their efficiency. The efficiency of a thermoelectric material is determined by its thermoelectric coefficient. The thermoelectric coefficient is a dimensionless figure of merit given as *ZT*, where $ZT = \alpha^2 T/\rho\kappa$ ($\alpha$ is the Seebeck coefficient (V $K^{-1}$), *T* the absolute temperature (K), $\rho$ the electrical resistivity ($\Omega$ cm), and $\kappa$ the thermal conductivity (W $cm^{-1}$ $K^{-1}$). As the value of *ZT* increases, so does the performance, or thermoelectric efficiency, of the material. Thus, the goal of researchers in this area is to maximize *ZT* throughout a

range of temperatures. This can only be done by minimizing the thermal conductivity while also maximizing the Seebeck coefficient and electrical conductivity of a given thermoelectric material. All three coefficients are closely coupled and depend strongly on the electronic structure, carrier concentration and crystal structure of a compound.[18]

For metals or degenerate semiconductors the Seebeck coefficient is the potential difference developed per unit temperature difference. It is proportional to the temperature and effective mass $m^*$ and inversely proportional to the charge carrier concentration $n$. On the hot side of a material, the concentration of electrons about the Fermi level is higher that on the cold side. The electrons will move from the higher energy hot side to the lower energy cold side. In order to maintain a temperature gradient, phonon exchange must be minimized. In the approximation of energy independent scattering, the equation for the relationship is[19]

$$\alpha = \frac{8\pi^2 k_B^2}{3e h^2} m^* \mathrm{T} \left(\frac{\pi}{3n}\right)^{\frac{2}{3}}, \qquad (1.1)$$

where $k_B$ is Boltzmann's constant, $e$ is the charge of an electron, and $h$ is Planck's constant.

Waste-heat is generated by all Carnot heat engines. As seen in Equation 2, in order to determine the theoretical maximum Carnot efficiency of a typical internal combustion engine, the temperature difference of the engine is divided by the hottest operating temperature:

$$\eta_{max} = \frac{\mathrm{T_{hot}} - \mathrm{T_{cold}}}{\mathrm{T_{hot}}} \qquad (1.2)$$

In theory, the hotter the engine can operate, more efficient it will be. Of course, the materials used to construct the engine, greatly limit the engines operating temperature.

With that said most of the heat produced by the engine is waste and dissipates in the surrounding environment directly next to the engine block or through the exhaust outlet.

In all automobiles with internal combustion engines, a percentage of the energy produced by the engine is used to power the alternator, which in turn recharges the vehicles' battery. The engines' power is also directly used to run the compressor on the vehicles' air conditioning unit and the power steering. Applying all three of these extra loads on the engine greatly reduces its efficiency. Finding a thermoelectric material that makes use of the waste-heat created by the engine, and generating the electricity needed to run one or all three of the above components will greatly increase the engines' efficiency and result in much better overall gas mileage for the vehicle.

Scientists began studying thermoelectric materials as early as the middle of the last century, with most of the initial research revolving around the space program. NASA needed a long-term, renewable energy source to power its long range space craft. Radioisotope thermoelectric generators were developed as thermal-to-electric conversion devises that powered certain unmanned space craft for up to 30 years.[1] Investigation into degenerate semiconductors lead to the discovery of other thermoelectric materials like $Bi_2Te_3$, PbTe, and Bi-Sb. Unfortunately, the ZT value of these materials never peaked much above 1.0 at any temperature. A plethora of other materials have since been discovered and have demonstrated potential thermoelectric properties. Many were synthesized using doping and forced-engineering methods and include complex structure compounds such at skutterudites, clathrates, and rare earth tellurides.[1] All of these materials' ZT values topped out at a relatively low

temperature, which did not make them practical for widespread applications. Then, in 2006, the discovery of $Yb_{11}MnSb_{11}$ started to shift some of the research in the direction of Zintl phases. Though $Yb_{11}MnSb_{11}$ does not have a record breaking ZT value, it achieved ZT > 1 at temperatures about 1200 K.[20]

In the past few years, our group has studied novel compounds for thermoelectric applications with a focus Zintl phases of *A*-*T*-*Pn* systems (*A* = alkaline- or rare-earth elements; *T* = Zn, Cd, Mn; *Pn* = pnictogen).[21-24] This paper reports more specifically on the *A*-Zn-*Pn* systems with new results on the synthesis and structural characterization of primitive hexagonal ZrBeSi (Pearson's symbol hP6) type structures. Metal-flux methods, using Zn and Pb as the flux, were used to synthesize ternary compounds $A_2$-$Zn_{2-x}$-$Pn_2$ where x≈1 (*A* = Eu, Sr; *Pn* = Sb, Bi). Upon characterization, the space group was determined to be $P6_3/mmc$. Madsen performed an automated band structure calculation of a select group of crystal structures in order to predict new thermoelectric materials.[18] Many of the structures he analyzed were narrow band gap semiconductors which contained Zn and Sb. LiZnSb[25] and KZnSb[26] are two of the compounds that Madsen analyzed when performing his automated search for potential thermoelectric materials. LiZnSb has the space group $P6_3mc$ (no. 186) and KZnSb has the space group of $P6_3/mmc$ (no. 194). Both crystals belong to the ternary transition metal pnictide class of Zintl compounds.[27] Looking at the structures of our proposed compounds, it appears there is a 50% occupancy at the Zn site. The Zn vacancies would allow for a stable electron count and provide proper ionic bonding between the Eu and $Zn_{1/2}Sb$ framework. These conjectures lead us to investigate the possibility that the unit cells formed a super-structure. The random

unfilled Zn sites could also provide the disorder needed to inhibit thermal conductivity. Since all reported compounds of the $A_2$-$Zn_{2-x}$-$Pn_2$ (x≈1) system solved with the same crystal structure, the super-structure speculation applied to all of the reported compounds. Electron diffraction was used on $Eu_2ZnSb_2$ to further verify the unit cell. A discussion of the TEM data as well as temperature dependant magnetism of $Eu_2ZnSb_2$ is presented in this paper.

# Chapter 2

# EXPERIMENTAL

## Synthesis

All materials were handled in an argon-filled glove box. The reported compounds were synthesized from reactions using pure elements from Alfa and Aldrich (>99.9%) as the starting materials. The reported samples were produced via flux reactions. The respective starting materials (alkaline-earth, transition metal, rare-earth metal, and pnictogens) were weighed in appropriate stoichiometric ratios and placed in 2 $cm^3$ alumina crucibles. Initially, each reaction was run using a 10-fold excess of Zn flux. It was noticed that in some of compounds, excess Zn was remaining in the crystal structures. It was then conjectured that Pb would a good flux due to its large size, low melting point and inertness. A 10-fold excess of Pb was then used as the flux. The crucibles were then enclosed in fused silica containers and flame-sealed under vacuum. The sealed mixtures were heated to 1000°C at a rate of 300°C per hour and allowed to remain at that temperature for 20 hours. The molten mixture was then cooled to 500°C at a rate of 20°C per hour. Once removed from the furnace, the samples were placed in a centrifuge in order to spin-off the flux and impurities, isolating the pure crystals. The fused silica containers were placed back in the argon-

filled glove box, where they were opened. Many single-crystalline grains with silver luster were observed with each reaction.

**Powder X-Ray Diffraction**

A Rigaku MiniFlex powder diffractometer (employing Cu Kα radiation) was used in order to identify initial reaction products. Each sample was prepared using the following technique. Within an Ar-filled glove box, a small number of crystals were ground to very fine powder using a mortar and pestle. The powder was then evenly distributed across the surface of a glass sample holder, that had a small amount of grease applied to it. The purpose of the grease was to allow the sample powder to adhere to the glass and remain immobile. After applying the powder, the sample holder was tilted and gently tapped to ensure all loose substances were removed. The sample holder was then sealed in a glass jar prior to removal from the glove box. This minimized the sample exposure to the atmosphere during transport to the diffractormeter. The diffractormeter was enclosed and operated inside a nitrogen-filled glove box. This also minimized the samples exposure to the atmosphere during the powder diffraction analysis. The title compounds contained elements that were highly reactive with oxygen and moisture. When the samples begin to oxidize and decompose, accurate data can not be obtained from the diffractometer. The sample remained in the glass jar during insertion to the diffractometer's glove box. The lid on the jar had to be opened slightly prior to being placed in the pump-down chamber to ensure a strong vacuum did not form within the jar. Once inside the sealed glove box, the sample holder was removed from the jar and placed in the diffractometer for

analysis. All diffraction patterns were taken at room temperature. The runs included $\theta$-$\theta$ scans with scan steps from 10-85 degrees at 0.05 degree increments and 5 seconds per step counting time. The JADE 6.5 program was used for data analysis of the compounds.[28] The analysis of the experimentally observed peaks corresponded well with those calculated from the crystal structures.

**Single-crystal X-Ray Diffraction**

Single-crystal X-Ray diffraction data were collected using a Bruker SMART CCD-based diffractormeter. The diffractometer used monochromated Mo $K\alpha$ radiation. Due to the air-sensitivity of the samples, all single crystals were selected in the glove box. Paratone N oil was used to cover the crystals prior to mounting them on glass fibers. The mounted crystals were quickly transferred onto the diffractometer's goniometer which was equipped with a liquid nitrogen evaporator. SMART was used for data acquisition using batch runs in different $\omega$ and $\varphi$ angles.[29] Data integration and refinement of the unit cell parameters were carried out with the SAINT program.[30] Semi-empirical absorption correction based on equivalents was applied using SADABS.[31] The SHELXL software package was used to determine the space group[32], while the structures were solved by direct methods and refined using the full matrix least-squared method on $F^2$.

**Electron Diffraction using TEM**

Transmission electron microscopy (TEM) studies were performed at the W.M. Keck Electron Microscopy Facility in the College of Engineering at the

University of Delaware. A JEOL-2000FX transmission electron microscope was used to execute the studies of the crystal structures. The TEM was operated at 200 keV and equipped with a LaB6 filament. At 200 keV, the filament emitted a current between 110 and 113 μA and the a point resolution of 2.9Å. Since the electron microscopy facility was located across the street from the chemistry laboratory, all samples had to be hand carried from one laboratory to the other. Care was taken to transport the samples as quickly as possible and minimize their exposure to air. $Eu_2ZnSb_2$ was found as the most air stable of all the crystal compounds. Therefore, it was the only crystal used in the TEM studies. Within an Ar-filled glove box, a small number of $Eu_2ZnSb_2$ crystals were ground using a mortar and pestle and then deposited on a lacey-carbon coated 300 mesh Cu-grid. Lacey-carbon coated grids were used in order to suspend the extremely small $Eu_2ZnSb_2$ particles that were deposited on the grid. The $Eu_2ZnSb_2$ particles were deposited on the grid by dipping the grid in the $Eu_2ZnSb_2$ powder.[33] The grid is then turned over to expel all large and loose particles that could potentially fall off inside the TEM. The remaining particles adhere to the grid through static forces. This method is somewhat crude since there is no guarantee how much of the compound will actually adhere to the grid. A more conventional method of mounting crystals is to grind the crystal and dissolve it in a solvent such as ethanol or acetone, and then apply a drop of the solution onto the grid. This method was initially tested, but upon analysis of the diffraction pattern, the $Eu_2ZnSb_2$ crystals reacted with the oxygen in the solvents and formed a polycrystalline structure, as illustrated in Figure 2.1.

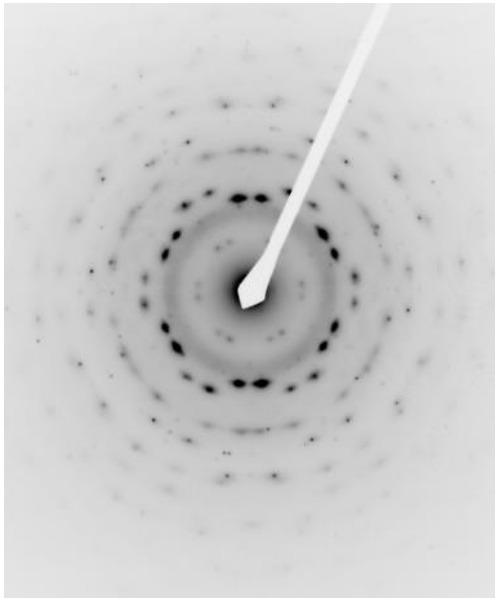

**Figure 2.1** Electron diffraction image of $Eu_2ZnSb_2$ after the compound was dissolved in acetone prior to placing on the TEM grid.

The grid was placed in a small plastic snap vile, sealed, and carried over to the TEM facility. Once at the facility, the grid was not removed from the vial until the double-tilt holder and TEM were fully prepped. Then, the grid was efficiently removed from the vile, mounted on the double-tilt holder, and inserted into the TEM. The sample was fully exposed to the atmosphere for less than two minutes. A double-tilt holder was used in order to adjust the sample in the both the *x* and *y* directions. This allowed the transmitted beam to strike the crystals at a variety of angles, producing diffractions images along different lattice planes. No adjustments were made in the *z* direction, as that was the camera length which was 80cm. Using an average magnification of x25,000, suitable pieces of the crystal sample were identified

for diffraction. These pieces were small and relatively thin, allowing the transmitted beam to go through the sample and reduce double diffractions. The diffraction aperture was then inserted into the beam path and the diffraction mode was set on the TEM. A small imaging screen and binoculars were used to view the fine diffraction spots. Images were focused and stigmatism was corrected using the corresponding controls on the TEM. Foot pedals were used to adjust the sample holder in the *x* and *y* directions. Once appropriate diffraction patterns were found, images of the electron diffraction patterns were recorded on film. The films were developed by the staff at the W.M. Keck Electron Microscopy Facility. The images were then scanned as saved as .TIF files in both a regular and inverted format for analysis using the JEMS (EMS Java) program.[34]

**Magnetic Susceptibility Measurements**

A Quantum Design MPMS-2 SQUID magnetometer was used to perform field-cooled *dc* magnetization (M) measurements. The measurements were conducted through temperatures ranging from 5 K to 290 K and an applied magnetic field (H) of 500 Oe. Holder contribution was taken into account through a raw magnetization data collection and converted to molar susceptibility ($\chi_m = M/H$).

**Element Analysis using EDS**

Inside of an argon-filled glove box large metallic crystals of $Sr_2ZnSb_2$ were crushed using a mortar and pestle, and mounted onto an Al stub using carbon tape. To ensure the entire compound adhered to the carbon tape, the sample holder

was turn upside down and tapped gently. Samples were imaged as prepared without additional conductive coating or grinding. Due to the air sensitivity of the compound and the geographical separation of the chemistry lab and microscopy facility, the sample holder was sealed in a small cap vial while still inside the glove box. The sealed snap vial was then transported to the W.M. Keck Electron Microscopy Facility in the College of Engineering at the University of Delaware. Once at the microscopy facility, the sample holder was quickly placed in a specimen holder and inserted into the chamber of a JEOL JSM 7400F scanning electron microscope. The sample was viewed on a digital screen at a magnification of x10,000. Once suitable areas on the sample were located, analysis was performed on two spots on two different crystals, for a total of four data collections. The composition of the sample was analyzed using the above mentioned SEM's INCA-OXFORD energy-dispersive spectrometer. During each analysis, the beam emission current of the microscope was 10 μA and the sample height was 8 mm. Setting the correct accelerating voltage is very important for the EDS detector. Having a general idea of the composition of the sample that is being analyzed is critical. The accelerating voltage must be set higher than the highest X-ray energy value of the elements in the sample. Many researchers recommend that throughout scanning, the accelerating voltage should be set at least twice as high as the largest Lα edge energy of the elements being analyzed. If the accelerating voltage is too low, the electron beam will not have enough energy to analyze all relevant X-ray energy values. Since the Lα edge energy values for Sr, Zn and Sb are 1.8 keV, 1.0 keV, and 3.6 keV, respectively, the accelerating voltage was set to 10 kV and the

probe current was held constant at 8 μA.[35] A 20μm$^2$ area was analyzed on each spot with a count time of 120 seconds for each run.

# Chapter 3

## RESULTS AND DISCUSSION

The crystal chemistry of many Eu-containing intermetallics is often parallel to that of the Sr. This is explained through the observation that Eu has a tendency to be present as $Eu^{2+}$ with a half-filled f-shell ($4f^7 6s^2$), rather than $Eu^{3+}$ ($4f^6$), which is typical for the other lanthanides trivalent state.[36, 37] Experiments performed with Eu, are usually repeated by substituting Sr, and vice-versa. Antimony containing Zintl compounds continue to be of great interest for their semiconducting properties. Some of these compounds include $Ca_{11}GaSb_9$,[38] $CaZn_2Sb_2$,[39] and $BaGa_2Sb_2$.[40] The title compounds are ternary rare-earth and transition metal pnictides that belong to a category of Zintl compounds. The $Eu^{2+}$ and $Sr^{2+}$ cations are considered as ions, positioned between the covalently bonded polyanionic sub-lattice of $[ZnPn_2]^{2-}$ (Pn = Sb, Bi), as illustrated by the unit cell representation in Figure 3.1.

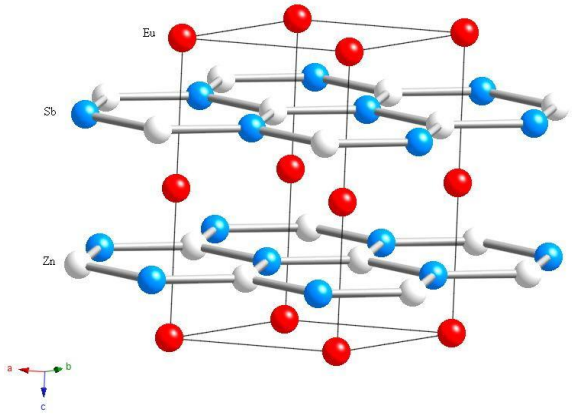


**Figure 3.1** Representation of the layered structure of $Eu_2ZnSb_2$ showing the Eu cations and [$ZnSb_2$] layers. All compounds in the series $Eu_2ZnPn_2$ (Pn = Sb, Bi) and $Sr_2ZnPn_2$ (Pn = Sb, Bi) have identical structures. Eu: Red spheres. Zn: White spheres. Sb: Blue spheres.

The cations provide the electrons for the bonding of the structure and fill the space between the sub-network layers. The sub-network layers can be characterized as anionic Zn-Pn sheets. Strongly covalent interactions are produced between the Zn and Pn atoms due to their similar electronegativities.[7]

As mentioned in the experimental section, the title compounds were each synthesized using two separate elements as the flux. Zn flux was initially used because it was already a part of the structures we were trying to form. On more than one occasion, the analysis of the powder X-ray diffraction data indicated we formed $EuZn_{13}$. As a cubic $NaZn_{13}$ structure type[41], $EuZn_{13}$ has already been reported from its powder X-ray diffraction,[42] as well as magnetic and thermoelectric properties.[43]

A powder X-ray diffraction analysis was performed on each of the compounds. The indexed XPD pattern for each of the compounds is shown in Figure 3.2.

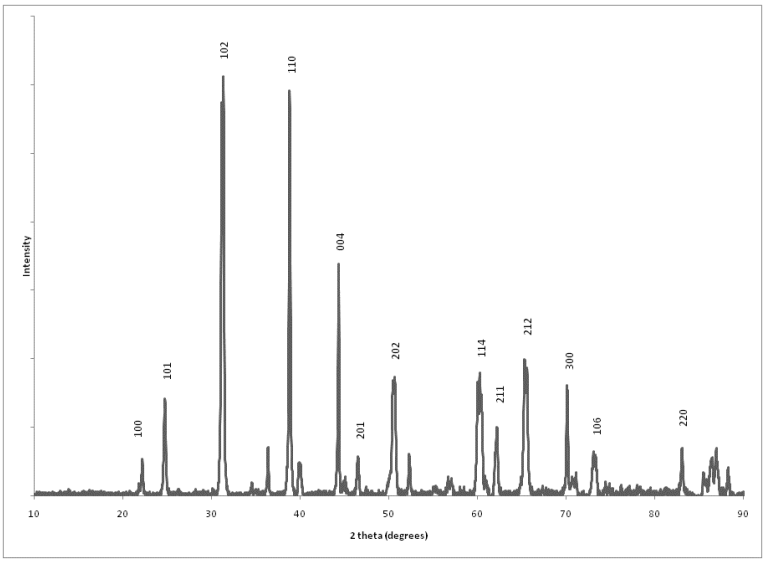


(A) $Eu_2ZnSb_2$

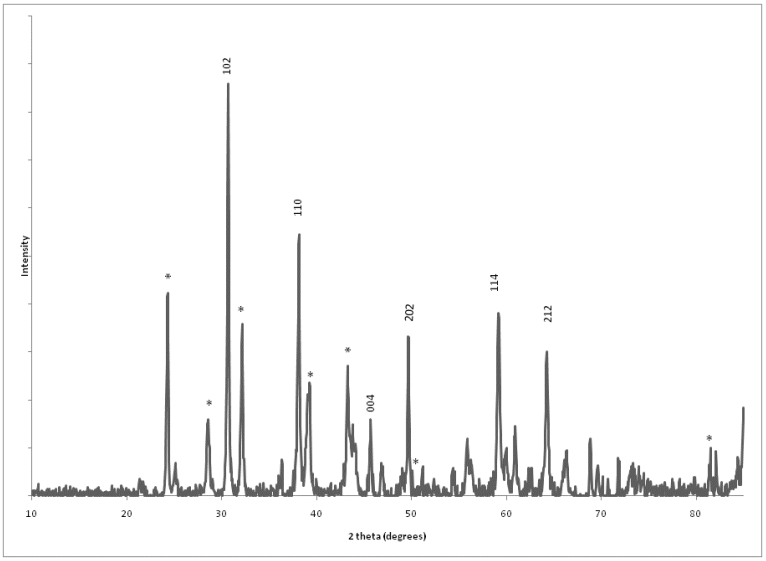


(B) $Eu_2ZnBi_2$

Note – The indexed XRD pattern of $Eu_2ZnBi_2$ together with $EuZnBi_2$ marked with *.

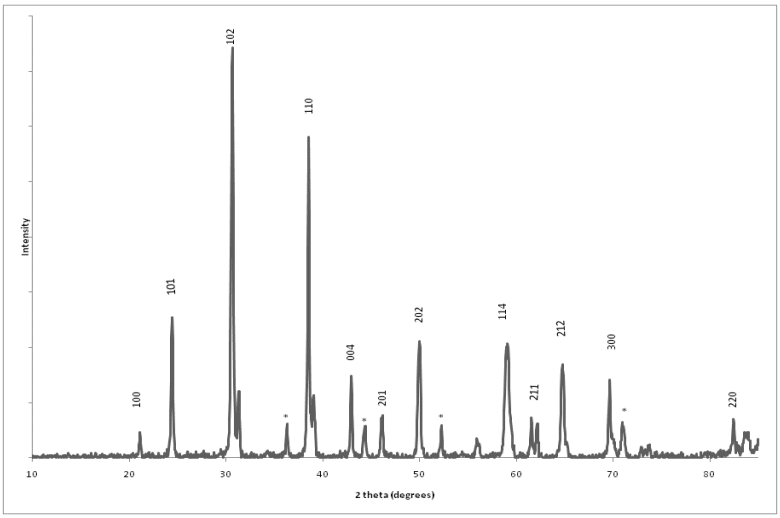


(C) $Sr_2ZnSb_2$

Note - The indexed XRD pattern of $Sr_2ZnSb_2$ together with $Zn_4Sb_3$ marked with *.

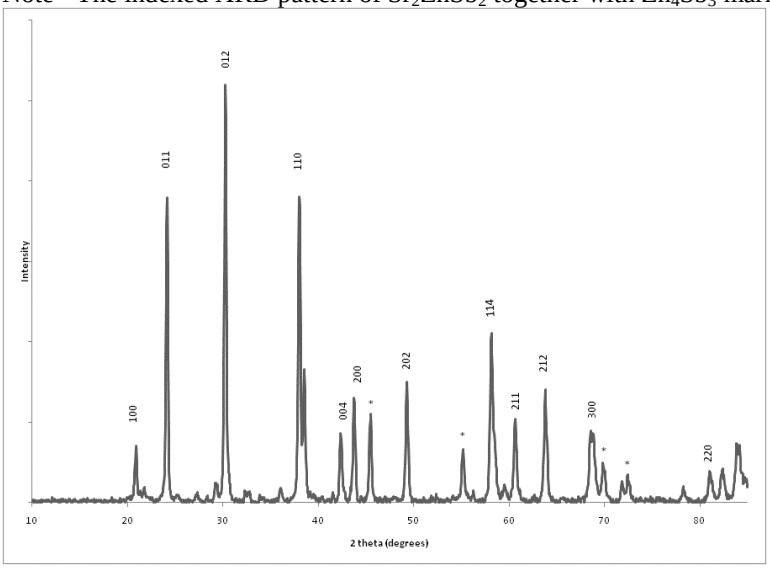


(D) $Sr_2ZnBi_2$

Note - The indexed XRD pattern of $Sr_2ZnBi_2$ together with $Bi_3Sr_5$ marked with *.

**Figure 3.2** Indexed X-ray powder diffraction patterns for (A) $Eu_2ZnSb_2$; (B) $Eu_2ZnBi_2$; (C) $Sr_2ZnSb_2$; (D) $Sr_2ZnBi_2$. The patterns for (B), (C), and (D) indicated impurities within the compounds.

Indexing the peaks and intensities of the powder X-ray diffraction patterns assigned each of the compounds with a hexagonal structure in $P6_3/mmc$. Powder X-ray diffraction analysis of the powder X-ray patterns for the compounds $Eu_2ZnBi_2$, $Sr_2ZnSb_2$, and $Sr_2ZnBi_2$ suggested some impurities within the compounds. The pattern for $Eu_2ZnBi_2$ also has peaks matching the compound $EuZnBi_2$. The $Sr_2ZnSb_2$ pattern has additional peaks matching those of the $Zn_4Sb_3$ compound. The final pattern showing $Sr_2ZnBi_2$ has peaks matching those of the $Bi_3Sr_5$ compound. After brief discussions with Dr. Susan Kauzlarich from the University of California-Davis, we attempted to complete the pnictogen series by synthesizing the ternary compounds $Eu_2$-Zn-$Pn_2$ (*Pn* = As, P) using similar reaction conditions and the same metal-flux technique. Though we synthesized compounds with the above elements, the analysis of the powder X-ray diffraction patterns indicated there were many impurities within the compounds.

The single crystal X-ray diffraction analysis provided much more detailed structure refinement information for the compounds, as seen in Table 3.1.

**Table 3.1** Selected crystal data and structure refinement parameters for $Eu_2ZnPn_2$ (Pn = Sb, Bi) and $Sr_2ZnPn_2$ (Pn = Sb, Bi).

| empirical formula | $Eu_2ZnSb_2$ | $Eu_2ZnBi_2$ | $Sr_2ZnSb_2$ | $Sr_2ZnBi_2$ |
|---|---|---|---|---|
| fw, g $mol^{-1}$ | 678.16 | 787.25 | 549.48 | 723.94 |
| space group | $P6_3/mmc$ (No. 194) | $P6_3/mmc$ (No. 194) | $P6_3/mmc$ (No. 194) | $P6_3/mmc$ (No. 194) |
| $\lambda$, Å | 0.7173 | 0.71073 | 0.71073 | 0.71073 |
| *T*, K | 120 | 120 | 120 | 120 |

| | | | | |
|---|---|---|---|---|
| *a*, Å | 4.635(1) | 4.701(1) | 4.623(1) | 4.728(1) |
| *c*, Å | 8.205(4) | 8.308(4) | 8.345(3) | 8.546(4) |
| *V*, Å$^3$ | 152.72 | 159.05 | 154.49 | 165.45 |
| *Z* | 1 | 1 | 1 | 1 |
| $\rho_{calcd,}$ g cm$^{-3}$ | 7.374 | 8.219 | 5.906 | 7.266 |
| μ (Mo Kα), mm$^{-1}$ | 36.51 | 78.13 | 33.25 | 75.99 |
| GOF on $F^2$ | 1.455 | 1.109 | 0.369 | 0.537 |
| $R_1$ [I>2σ(I)] | 0.0342 | 0.0384 | 0.0139 | 0.0280 |
| $wR_2$ [I>2σ(I)] | 0.0951 | 0.0546 | 0.0452 | 0.0583 |
| $R_1$ [all data] | 0.0470 | 0.0430 | 0.0204 | 0.0338 |
| $wR_2$ [all data] | 0.0247 | 0.0546 | 0.0452 | 0.0583 |

**Table 3.1 Cont.**

Table 3.2 and Table 3.3 list the atomic coordinates and isotropic displacement parameters, as well as interatomic distances.

**Table 3.2** Atomic coordinates and equivalent isotropic displacement parameters (*U*eq[a]) for $Eu_2ZnPn_2$ (Pn = Sb, Bi) and $Sr_2ZnPn_2$ (Pn = Sb, Bi).

| Atom | Site | *x* | *y* | *z* | $U_{eq}$ (Å$^2$) |
|---|---|---|---|---|---|
| | | $Eu_2ZnSb_2$ | | | |
| Eu1 | 2*a* | 0 | 1 | 0 | 0.022(1) |
| Zn | 2*d* | 2/3 | 1/3 | ¼ | 0.032(4) |
| Sb1 | 2*c* | 1/3 | 2/3 | ¼ | 0.014(1) |
| | | $Eu_2ZnBi_2$ | | | |
| Eu1 | 2*a* | 0 | 1 | 0 | 0.031(6) |
| Zn | 2*d* | 2/3 | 1/3 | ¾ | 0.046(3) |
| Bi1 | 2*c* | 1/3 | 2/3 | ¼ | 0/026(6) |
| | | $Sr_2ZnSb_2$ | | | |
| Sr1 | 2*a* | 0 | 1 | 0 | 0.019(4) |
| Zn | 2*d* | 2/3 | 1/3 | 1/4 | 0.013(1) |
| Sb1 | 2*c* | 1/3 | 2/3 | 1/4 | 0.011(4) |
| | | $Sr_2ZnBi_2$ | | | |
| Sr1 | 2*a* | 0 | 1 | 0 | 0.018(7) |
| Zn | 2*d* | 2/3 | 1/3 | 1/4 | 0.013(2) |
| Bi1 | 2*c* | 1/3 | 2/3 | 1/4 | 0.012(5) |

**Table 3.3** Interatomic distances (Å) for $Eu_2ZnPn_2$ (Pn = Sb, Bi) and $Sr_2ZnPn_2$ (Pn = Sb, Bi).

| Atom Pair | $Eu_2ZnSb_2$ | Atom Pair | $Eu_2ZnBi_2$ | Atom Pair | $Sr_2ZnSb_2$ |
|---|---|---|---|---|---|
| Eu – Zn (6x) | 3.3722(9) | Eu – Zn (6x) | 3.418(1) | Sr – Zn (6x) | 3.3879(8) |
| Eu - Sb (6x) | 3.3722(9) | Eu – Bi (6x) | 3.418(1) | Sr – Sb (6x) | 3.3879(8) |
| Zn – Sb (3x) | 2.6765(7) | Zn – Bi (3x) | 2.714(1) | Zn – Sb (3x) | 2.6693(7) |

| Atom Pair | $Sr_2ZnBi_2$ |
|---|---|
| Sr – Zn (6x) | 3.4664(9) |
| Sr – Bi (6x) | 3.4664(9) |
| Zn – Bi (3x) | 2.7297(7) |

The single crystal data confirms the unit cell parameters and determined the space group ($P6_3/mmc$). The bond lengths within the compounds are consistent with the size of the atoms. The compounds containing Bi atoms have longer bonds than the compounds containing Sb atoms. This makes sense because Bi is located one period below Sb, and is a larger atom. The covalent bonds within the polyanionic sub-lattices $[ZnPn_2]^{2-}$ are within reason of previously calculated values. The $d_{Zn\text{-}Sb}$ within $Eu_2ZnSb_2$ and $Sr_2ZnSb_2$ are 2.6765(7) Å and 2.6693(7) Å, respectively. These numbers are slightly shorter than the sum of the corresponding covalent radii of $d_{Zn\text{-}Sb} \approx 2.72$Å.[44] For the compounds $Eu_2ZnBi_2$ and $Sr_2ZnBi_2$, the $d_{Zn\text{-}Bi}$ are 2.714(1) Å and 2.7297(7) Å, respectively. These values are also slightly shorter than the sum of the corresponding covalent radii of $d_{Zn\text{-}Bi} \approx 2.77$Å.[44] Sr atoms have slightly larger atomic radii than do Eu atoms, therefore it makes sense that the crystal structures and bond distances containing Sr are slightly larger than those with Eu. These distances compare

well with those reported for other compounds containing the same elements: $d_{Zn\text{-}Sb}$ = 2.658 Å in $Eu_{13}Zn_6Sb_{12}$,[21] and $d_{Zn\text{-}Bi}$ = 2.8569 Å in $Ba_2ZnBi_2$.[45]

An interesting feature of the title compounds' structures are their relationship to the hypothetical compounds AZnPn (A = Sr, Eu and Pn = P, As, Sb, Bi). The structure solutions in the space group $P6_3/mmc$ suggest a ZrBeSi type structure, which in turn represents the filled nickel arsenide structure.[46] Other intermetallic phases are known to crystallize with this all-pervading type, including KZnSb.[26] KZnSb is an electronically stable 1:1:1 compound with an electron count of $K^+Zn^{2+}Sb^{3-}$. The four compounds synthesized in this experiment have the same structure and space group as KZnSb. Using the empirical rules of formal charge, the electron count for EuZnSb is understood as $Eu^{2+}Zn^{2+}Sb^{3-}$, and would hold true for the other three compounds when substituting in the respective elements. It is a fact that no equiatomic compounds of the alkaline-earth, group 12 transition metal, and the pnictogens have been discovered.[47] This creates an unbalance of charges because the compound is excess electrons; leading to an electronically unstable compound. A structural rearrangement is required so that the effect of the antibonding states is diminished.[10] There are two methods that would satisfy this rearrangement. One method is a long range anionic vacancy. The other method is the exclusion of a cation. The anionic vacancy would arise due to the removal of one-half of the Zn atoms, thereby creating a 50% vacancy within the structures. The 50% occupancy opens the possibility for an ordered superstructure with a two-times larger unit cell. It would be considered a defect in the structure. The exclusion of a cation (Eu/Sr) would change the overall bonding and structure of the compounds. Holes in the cationic layers would

disrupt the ionic bonding within the structure. Single crystal X-Ray diffraction measurements confirm the position of the Eu/Sr atoms. Therefore, it can be deducted that the Zn atom produces random absences during ordering. A 50% partial occupation by the Zn atom would attain an electron count of $Eu^{2+}Zn^{+}Sb^{3-}$. This configuration allows for an electronically favored compound. The long range vacancy order leads to a larger unit cell than predicted, as shown in Figure 3.3. The black rectangles represent the unit cell.

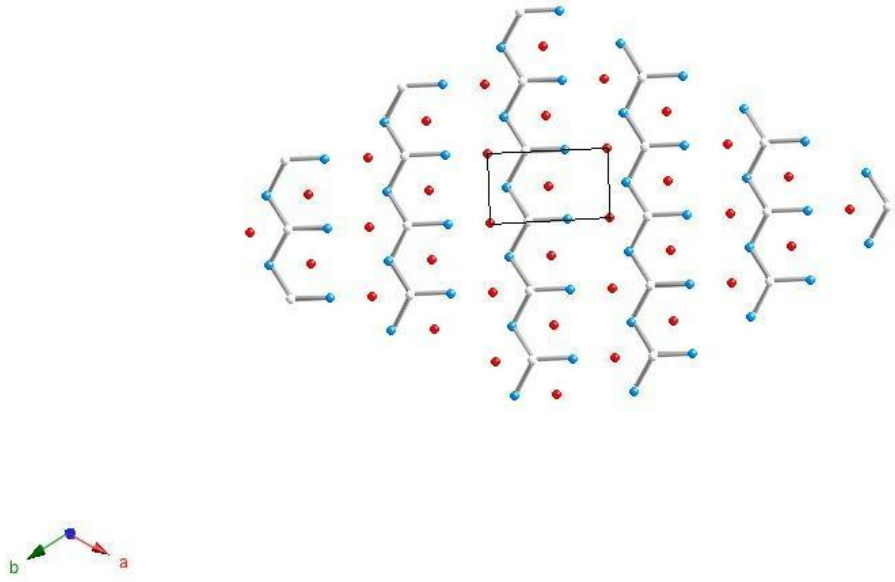

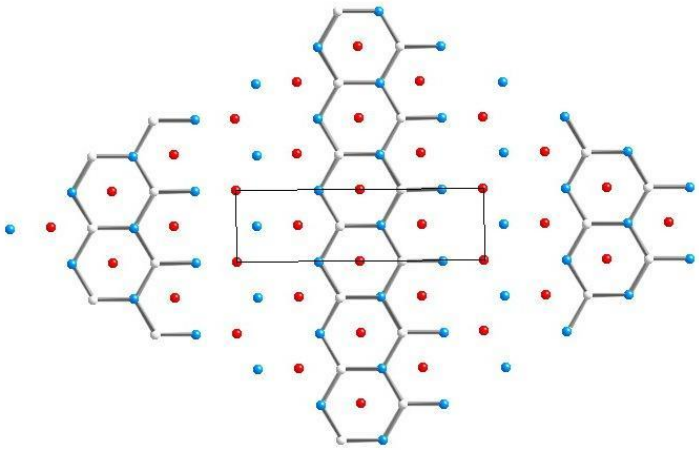

**Figure 3.3** Two possible representations of the $Eu_2ZnSb_2$ crystal structure with Zn vacancies ordered in different ways. The black rectangles represent the unit cell. The views are from the *c*-direction, with the Eu atoms visible. Eu: Red spheres. Zn: White spheres. Sb: Blue spheres.

We used the TEM to study the possible order within the crystal compounds. If there were vacancies in the structures, the electron diffraction images would illustrate the superstructures by the two times larger unit cell. If spots appear when diffraction is performed on a specimen in a TEM, it means that specimen is at least partially crystalline. TEMs have the ability to determine crystallographic orientations down to the nm level. Electron diffraction typically deals with positions of the spots rather than their intensities because the electron beam is diffracted many times in a typical TEM specimen.[48] In a TEM, many diffracted beams are visible with a single wavelength. Electron beams are easily directed because electrons are charged particles. Electrons also scatter very strongly in sample because they interact with both the nucleus as well as other electrons of the scattering atom.

Whether or not a diffracted wavefront corresponds to a diffracted beam depends on whether the atoms are scattering in phase. This is ultimately determined by the angles between the incident beam, the diffracted beam and the diffracting planes. The conditions for individual waves being in phase are the Laue conditions. Providing that the energy of an electron is unchanged during diffraction, the scattering process is elastic. During electron diffraction, two beams are scattered from two points, which lie on different planes. The path difference that the rays travel is the basis for the Bragg Law

$$n\lambda = 2d \sin \theta. \tag{3.1}$$

The Bragg angle is the most important scattering angle in TEM because at that exact angle the electron waves interfere constructively, thus creating a diffraction pattern. Typically, the Bragg angle of interest is less than 1º. It does not matter how many atoms are located on a plane, Bragg's Law indicates that there is no path difference for their scattering. The Bragg reflection is perpendicular to the set of planes. When the electrons are diffracting from a set of planes with spacing *d*, the *n* in the Bragg equation indicates that the electrons are diffracting from planes with spacing that is actually *d/n*.

The zone axis [*UVW*] is the direction along the intersection of two or more planes and is the direction which is common to all the planes of the zone. [*UVW*] is also perpendicular to (*hkl*) if the plane is in the [*UVW*] zone. This defines the Weiss zone law: $hU+kV+lW=0$.

Single crystals form images of discrete dots that are usually arranged in a geometric shape. This is called the reciprocal lattice. The fundamental relationship for diffraction patterns remains the same at R$d$=$\lambda$L. Where any distance R that is measured on the diffraction pattern is related to a specific spacing in the crystal, $d$. Since $\lambda$L is constant, measuring several values of R will yield the result R1d1=R2d2=R3d3… This means that ratio of any two R values gives the ratio of the d-spacing. If the lattice parameters of the sample crystal are known, then the allowed reflections can be determined and certain d-spacings will be associated with the diffraction spots. Once values for **g**1 and **g**2 are known, the answers are cross-checked using the angles between the **g** vectors.

TEM images of the electron diffraction patterns for $Eu_2ZnSb_2$ further verify the unit cell calculations for the compounds. Manually measuring the distance between the transmission beam and spot reflections in Figure 3.4 gave all measurements as equal distant. Knowing the hexagonal structure of the compound, it was determined that the electron diffraction pattern was imaged in a [001] zone axis.[49] The brighter spots around the origin are second order scattering. The weak spots around the middle of the image indicate a strong possibly of a larger unit cell. This would lead to the conclusion that a super-lattice is present. The center of the images is very bright, causing some of the weak diffraction spots not to show up on the micrograph. To alleviate the problem, the camera length should be increased from 80 cm to at least 100 cm. This will decrease the intensity of the beam when it strikes the sample, and allow the diffraction pattern in the middle to be visible.

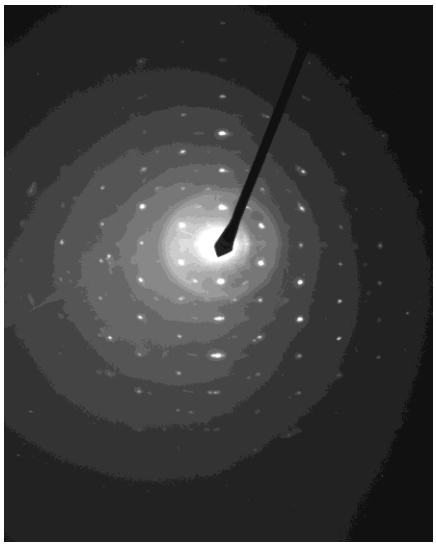

(A)

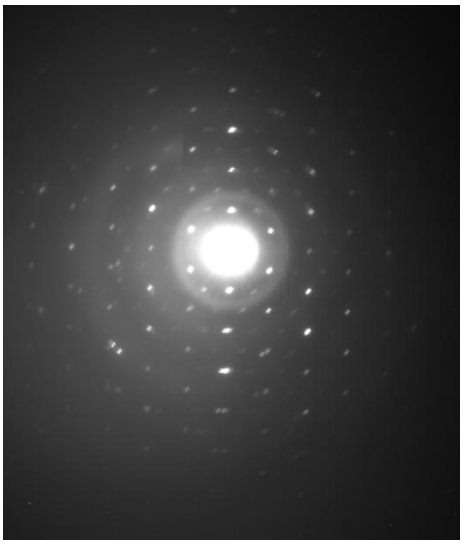

(B)

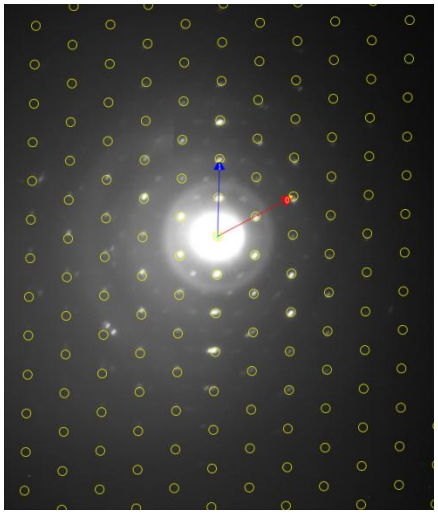

(C)

**Figure 3.4** **[**001] SAED patterns of $Eu_2ZnSb_2$. (A) shows the diffraction pattern using the beam block, (B) is the same pattern without the beam block, (C) is the same pattern with the base arrows and mask overlay applied that is used by the JEMS program to index the pattern.[34]

JEMS is a JAVA based computer program that performs automated electron diffraction indexing. First, the $Eu_2ZnSb_2$ crystal structure was entered in the program. The unit cell parameters, space group and atom positions were all defined in building the structure. Once the crystal structure was built in the program, those parameters were used as a basis for indexing the associated diffraction pattern. One of the .TIF files from the scanned images was then loaded into the program. Many constants were then entered into the program to include the camera length (800mm), accelerating voltage (200kV), and the distance between the origin, transmitted beam and a reflection (this value was measured on the actual micrograph in mm). The program then overlaid a mask on the image and the image was then calibrated. JEMS calculated the distances to the two second order spots (Figure 3.5C) as 2.28 Å and 2.49 Å. The angle between the spots was calculated at 62.2º. Auto indexing began to find a possible zone axis using the crystal structure file that was built and the image that was loaded. A stereographic projection was displayed showing the zone axis found using the lattice parameter of the crystal file. Figure 3.5 shows the indexed pattern for the [001] zone axis created by the JEMS programs.[34]

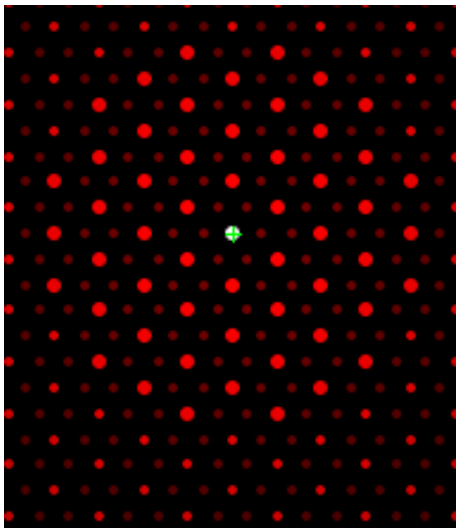

**Figure 3.5** A simulated indexed diffraction patterns created by JEMS from the images in Figure 3.4. JEMS solved for the [001] zone axis.

This indexed diffraction pattern matches the film images created by the $Eu_2ZnSb_2$ electron diffraction pattern. Comparing the actual images to the simulated image, they appear to be a good match. Though the center of the film images is very bright, a similar pattern is observed between the bright and weak reflections. The weak spots in the middle of the simulated image created my JEMS further shows the possible presence of a larger unit cell.

The electron diffraction pattern image in Figure 3.6 shows a different zone image of the $Eu_2ZnSb_2$ structure. This image was taken along the [010] zone axis and shows a contrast between bright and weak reflections.

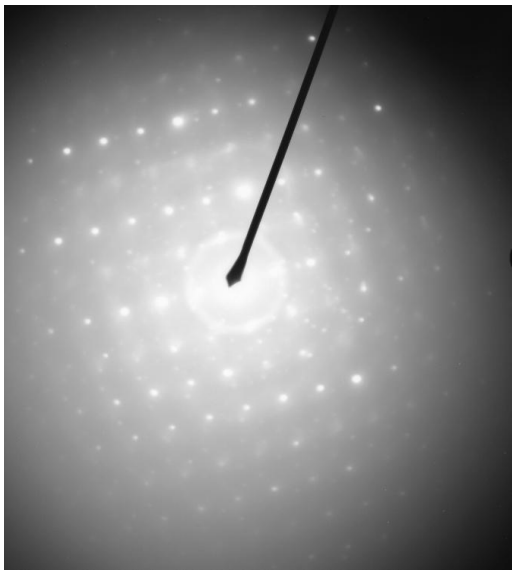

**Figure 3.6** SAED image along the [010] zone axis for $Eu_2ZnSb_2$.

Once again, the center is very bright, causing some of the diffraction spots not to show up on the micrograph. The images obtained from the TEM did not provide evidence there are long range Zn vacancies. The initial goal was to produce images that clearly illustrated a larger unit cell. The electron diffraction patterns alone do not prove a super-lattice caused by unfilled occupancy sites from the Zn atoms, but they do provide some evidence that justifies that conjecture.

The X-Ray Energy-Dispersive Spectrometer is a powerful, yet user friendly detector that allows the user to identify or verify the composition of a given sample. EDS produces a spectrum that plots the X-ray counts versus the X-ray energy of a material. A computer program then analyzes this data to determine what elements compose the sample being analyzed.

As with all SEMs, an electron beam is produced and is focused on the sample. Electrons from the beam strike the sample and excite electrons within it. Some of these excited electrons have enough energy to jump from their respective orbital up to the element's conduction band, leaving an empty slot in the orbital they left. An electron from a higher orbital will then drop down into the lower orbital, filling the vacancy. This electron loses energy and gives off the lost energy in the form of a characteristic X-ray. It is these X-rays that are usually detected by the XEDS detector. For each atom, every shell has a unique energy level determined by the atomic configuration for that element. Depending on which shell an electron moves from, determines the energy of the X-ray. This allows characteristic X-ray energies to be unique. The energy levels for the atomic shells increase as you get closer to the nucleus, showing Kβ>Kα>L>M.[50] The change in energy is calculated using the following equation:

$$\Delta E = \frac{-kZe^2}{2}\left(\frac{1}{ri} - \frac{1}{rf}\right) \tag{3.2}$$

The X-rays are detected by a silicon-lithium [Si(Li)] semiconductor detector. Incoming X-rays interact with the semiconductor and cause electrons from the silicon to be transferred from the valence band to the conduction band. This creates on electron-hole pair within the semiconductor. The number of electron-hole pairs is directly proportional to the energy of the incoming X-rays. The corresponding signal emitted by these electron-hole pairs is then analyzed and used to distinguish elements in the sample. As the atomic number increases, so does the K shell line energy. It is possible for signals from some shells to be too weak to be detected. Peak overlap also

occurs, especially at the low energy end and with elements that have smaller atomic numbers. Commercially manufactured Si is not intrinsic and contains acceptor impurities. This causes the Si to act as a p-type semiconductor. Over time, the Si would suffer electrical breakdown when a bias was applied to separate the electrons from the holes. To compensate for the impurities, Li is used to fill recombination sites, creating a region of intrinsic Si. The addition of Li accounts for a more complete bonding of the silicon, which increases the signal to noise ratio.[50]

Often times, EDS spectrum show artifacts. These artifacts are separated into two groups. The first group is signal-detection artifacts, these include escape peaks and internal-fluorescence peaks. The second group is signal-processing artifacts which include sum peaks.

Escape peaks occur when some of the X-ray energy is lost and not transformed to electron-hole pairs. This often happens when the incoming photon of energy fluorescence a Si Kα X-ray, and then gets registered by the detector at 1.74keV. Escape peaks usually appear in the spectrum 1.74keV below the major characteristic peak position.[50]

Internal-fluorescence occurs in the Si detector dead layer. Small Si peaks are seen in almost all spectra. The longer the counting time for the spectra, the more prominent the internal-fluorescence peak will be. A small peak forms on the spectrum at 1.74keV, the Si Kα X-ray energy.[50]

Sum peaks arise when the electronics of the devise are not fast enough. When two photons enter the detector simultaneously, the analyzer will register the energy corresponding to the sum of the two photons. The sum peak usually appears at

twice the energy of the major peak, when the count rate is high, and when dead times are in excess of 60%.[50]

The EDS program on the JEOL JSM 7400F electron microscope measured the weight percent and atomic percent of each element in the $Sr_2ZnSb_2$ compound. The averaged atomic percentages of the elements Sr, Zn, Sb were 39.81%, 20.25%, and 39.94%, respectively. The 2:1:2 measurements further verifies that our previous formula is correct.

After performing multiple analyses to determine and verify the structure of the compounds, it was time to perform a property measurement on $Eu_2ZnSb_2$. Measuring the magnetic susceptibility of the compound would determine its magnetic behavior as well as clarify whether Eu was in the divalent or trivalent state.

The electronic configuration of Eu, $4f^7 6s^2$, is that of a half-filled 4f-orbital that can potentially lead to novel magnetic phenomena.[51] Specifically, strong magnetic effects are directly associated with charge fluctuations because divalent Eu is in the pure spin state ($L = 0$), while trivalent Eu is non-magnetic ($J = 0$).[51] The plot of the temperature dependence of the magnetic susceptibility $\chi = M/H$ for the single-crystal of $Eu_2ZnSb_2$ is shown in Figure 3.7.

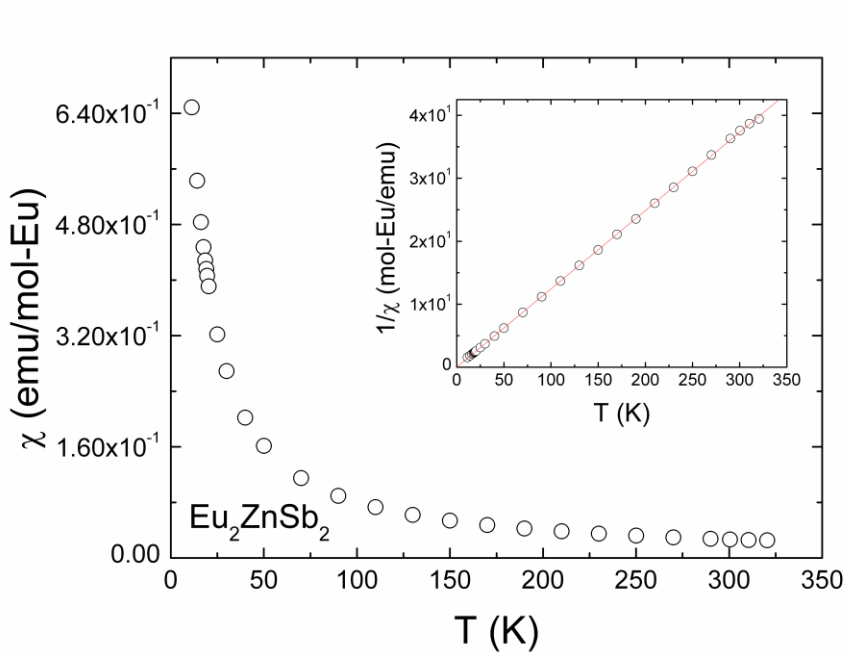


**Figure 3.7** Temperature dependence of the magnetic susceptibility of $Eu_2ZnSb_2$ single-crystals. The inverse of the magnetic susceptibility ($\chi^{-1}$) plot with corresponding linear fit curve are shown in the inset.

The graph of $\chi(T)$ follows the Curie-Weiss law $\chi(T) = C/(T - \theta_P)$, where $C = N_A\mu_{eff}^2/3k_B$ is the Curie constant and $\theta_P$ is the Weiss temperature.[21,52] Above 50 K, the inverse of the magnetic susceptibility $(\chi^{-1})$ shows a linear dependence on T and the compound exhibits paramagnetic behavior. Using linear fit to extrapolate the data, and effective moment of $\mu_{eff} = 8.01\ \mu_B$ per $Eu^{2+}$ ion was calculated. This value agrees well with the theoretical value of $\mu_{eff} = 7.94\ \mu_B$ per $Eu^{2+}$ ion[21,52] (the expected value for the $Eu^{3+}$ ion is $\mu_{eff} = 0\ \mu_B$). The Curie-Weiss temperature was calculated as $\theta_{CW} = -0.39$ K. The negative number indicates possible anti-ferromagnetic ordering at very low

temperatures. The Neel temperature is not observed in the graph due to measurements not being conducted at temperatures below 10 K. The above data further confirms the divalent state of Eu in this structure and that the formula of the 2:1:2 compounds are correct.

# Chapter 4

## CONCLUSION AND FUTURE WORK

The new intermallic compounds reported all have a hexagonal lattice structure and $P6_3/mmc$ space group. It is proposed that the structures have a 2:1:2 formula. Though the initial electron count for the structures adds up to an excess of electrons, the crystal structure has been confirmed using powder X-ray diffraction and single-crystal X-ray diffraction. Data obtained from the EDS further verified the 2:1:2 structures through measurements of atomic ratios within the compounds. Electron diffraction results were inconclusive in regards to Zn vacancies within the structures, based on the images obtained. However, electron diffraction did confirm the unit cell. Magnetic susceptibility experiments measured Eu as divalent within the compounds. This strong evidence suggests that to offset the unbalanced electronic state, there must be a partial occupancy by the Zn atom. A 50% occupancy at the Zn site leads to a balanced electronic state. It can be reasoned that the reported structures have a potential to hold thermoelectric properties. Other compounds with the same lattice structure and space group are predicted to be narrow band-gap semiconductors based off of their band structure calculations. Therefore, the reported compounds should have similar band structure calculations. The random vacancies of the Zn atoms are a positive aspect because they add disorder to the crystal structures which would lower

thermal conductivity in the material by reducing phonon exchange at higher temperatures. Further experiments to complete the pnictogen series may prove valuable. Synthesizing the 2:1:2 phase of the As and P containing compounds will probably require changing some of the reaction conditions to include the initial ratios of the elements and the temperature profiles. Future measurements should also be performed to verify thermoelectric properties. These include measuring electrical resistivity, thermal conductivity and the Seebeck coefficient in order to calculate the thermoelectric coefficients of the crystal structures.

## REFERENCES


1. Fleurial, J.P. *J. of Min. Met. And Mat. Soc*. **2009**, *61*, 79.

2. *Atomic Power in Space: A History*, Report, DOE/NE/32117-H1. Washington, D.C.: U.S. Department of Energy, **1987**.

3. Hall, W.C. in CRC Handbook of Thermoelectrics, ed. D.M.Rowe, CRC Press, Boca Raton, FL, **1995**, 40, 503-513.

4. Guazzoni, G. "Thermoelectric Generators for Military Applications," Proc. 4th Int. Conf. on Thermoelectrics. Arlington, TX, **1982**, 1-6.

5. Nolas, G.S. *Appl. Phys. Lett.* **1998**, *73*, 178.

6. Slack, G.A. in CRC Handbook of Thermoelectrics, ed. D.M.Rowe, CRC Press, New York, **1995**, 407.

7. Kauzlarich, S.M.; Brown, S.R.; Snyder, G.J. *Dalton Trans*. **2007**, 2099.

8. Zintl, E. *Angew. Chem*. **1939**, *52*, 1.

9. Mudring, A.V.; Corbett, J.D. *J. Am. Chem. Soc*. **2003**, *126*, 5277.

10. Xai, S.-Q.; Bobev, S. *J. Am. Chem. Soc*. **2007**, *129*, 4049 - 4057.

11. (a) Schafer, H.; Eisenmann, B.; Muller, W. *Angew, Chem., Int. Ed. Engl*. **1973**, *12*, 694 – 712. (b) Corbett, J.D. *Angew. Chem., Int. Ed.* **2000**, *39*, 670 – 690.

12. (a) Kauzlarich, S.M. Ed. Chemistry, Structure and Bonding in Zintl Phases and Ions; VCH: New York, **1996**, and the references therein. (b) Miller, G.J.; Eur. J. *Inorg. Chem*. **1998**, 523 – 536.

13. Nesper, R. Angew. *Chem., Int. Ed. Engl*. **1991**, *30*, 789-817.

14. (a) Gascoin, F.; Sevor, S.C. *Angew. Chem., Int. Ed.* **2002**, *41*, 1232 – 1234. (b) Gascoin, F.; Sevor, S.C. *Inorg. Chem.* **2002**, *41*, 2820 – 2825. (c) Gascoin, F.; Sevor, S.C. *Inorg. Chem.* **2002**, *41*, 5920 – 5924. (d) Gascoin, F.; Sevor, S.C. *Inorg. Chem.* **2002**, *41*, 904 – 907.

15. (a) Kuromota, T.Y.; Kauzlarich, S.M.; Webb, D.J. *Chem. Mater.* **1992**, *4*, 435 – 440. (b) Kim, H.; Condron, C.L.; Holm, A.P.; Kauzlarich, S.M. *J. Am. Chem. Soc.* **2000**, *122*, 10720 – 10721. (c) Holm, A.P.; et. at. *J. Inorg. Chem.* **2003**, *42*, 4660 – 4667. (d) Holm, A.P.; Olmstead, M.M.; Kauzlarich, S.M. *Inorg. Chem.* **2003**, *42*, 1973 – 1981. (e) Jiang, J.; et. al. *Inorg. Chem.* **2005**, *44*, 2189 – 2197. (f) Brown, S.R.; et. at. *Chem. Mater.* **2006**, *18*, 1873 – 1877.

16. (a) Chung, D.Y.; et. at. *Science*. **2000**, *287*, 1024 – 1027. (b) Kim, S.J.; et. at. *J. Am. Chem. Soc.* **2001**, *123*, 12704 – 12705. (c) Park, S.M.; Kim, S.J.; Kanatzidis, M.G. *Inorg. Chem.* **2005**, *44*, 4979 – 4982.

17. (a) Bobev, S.; et. at. *Inorg. Chem.* **2004**, *43*, 5044 – 5052. (b) Bobev, S.; et. al. *Inorg. Chem.* **2006**, *45*, 4047 – 4054. (c) Xia, S.-Q.; Bobev, S. *Inorg. Chem.* **2007**, *45*, 7126 - 7132. (d) Xia, S.-Q.; Bobev, S. *Inorg. Chem.* **2007**, *46*, 874 – 883.

18. Madsen, G.K.H. *J. Am. Chem. Soc.* **2006**, *128*, 12140.

19. Zhang, H.; et al. *J. of Chem. Physics*. **2008**, *129*, 164713.

20. Brown, S.R.; et. al. *Chem. Mat.* **2006**, *18*, 1876.

21. Saparov, B.; et. al. *J. of Solid State Chem.* **2008**, *181*, 2690 – 2696.

22. Saparov, B; Xia, S.-Q.; Bobev, S. *Inorg. Chem.* **2008**, *47*, 11237 – 11244.

23. Xia, S.-Q.; Myers, C; Bobev, S. *Eur. J. Inorg. Chem.* **2008**, 4262 – 4269.

24. Xia, S.-Q.; Bobev, S. *J. of Comp. Chem.* **2008**, *29*, 2125 – 2133.

25. Schroeder, G.; Schuster, H. Z. *Naturforsch., B: Anorg. Chem., Org. Chem.* **1975**, *30*, 978 – 979.

26. Savelsberg, G.; Schaefer, H. Z. *Naturforsch., B: Anorg. Chem., Org. Chem*. **1978**, *33*, 370 – 373.

27. Nesper, R. *Prog. Solid State Chem*. **1990**, *20*, 1 - 45.

28. JADE Version 6.5, Materials Data, Inc., Livermore, CA, 2003.

29. SMART NT Version 5.6, Bruker Analytical X-ray Systems, Inc., Madison, WI, 2003.

30. SAINT NT Version 6.4, Bruker Analytical X-ray Systems, Inc., Madison, WI, 2003.

31. SADABS NT Version 2.1, Bruker Analytical X-ray Systems, Inc., Madison, WI, 2003.

32. SHELXTL Version 6.1, Bruker Analytical X-ray Systems, Inc., Madison, WI, 2003.

33. Pyrz, W.D.; Buttrey, D.J. *Langmuir*. **2008**, **24**, 11350 – 11360.

34. JEMS (EMS Java) Version 3.0308W2006, Electron Microscopy General, Copyright Pierre Stadelmann, 1999-2006.

35. Kortright, J.B. and Thompson, A.C. X-Ray Data Booklet: Section 1.2 X-ray Emission Energies, Table 1-2.

36. Gschneider Jr., K.A.; Eyring, L. (Eds.) Handbook on the Physics and Chemistry of Rare Earths, Vol, 2, North Holland, Amsterdam, **1979**.

37. Saparov, B.; Bobev, S. *J. of Alloy and Comp*. **2008**, *463*, 119 – 123.

38. Young, D.M.; Kauzlarich, S.M. *Chem. Mater*. **1995**, *7*, 206 – 209.

39. Gascoin, F.; et al. *Adv. Funct. Mat*. **2005**, *15*, 1860.

40. Kim, S.J.; Kanatzidis, M.G. *Inorg. Chem*. **2001**, *40*, 3781 – 3785.

41. Massalski, T.B. (Ed.) Binary Alloy Phase Diagrams, 2nd ed., American Society for Metals, Materials Park, OH, **1990**.

42. Iandelli, A.; et. al. *Less-Common Met.* **1967**, *12*, 333.

43. Buschow, K.H.J.; et. al. *Phys. G: Met. Phys.* **1975**, *5*, 1625 – 1636.

44. Speight, J.G. Lange's Handbook of Chemistry (16th Edition); McGraw-Hill, **2005**.

45. Saparov, B.; Bobev, S. *Inorg. Chem*. **2010**, *49*, 5173 - 5179.

46. Nielsen, J.W.; Baenziger, N.C. *Acto Cryst*. **1954**, *7*, 132.

47. (a) Villars, P.; Calvert, L.D. Pearson's Handbook of Crystallographic Data for Intermetallic Phases, 2nd ed.; American Society of Metals: Materials Park, OH, **1991**, and the desktop edition, **1997**. (b) Inorganic Crystal Structure Database, Fachinformationszentrum (FIZ) Karlsrube.

48. Williams, D.B.; Carter, C.B. Transmission Electron Microscopy; Springer Science Business Media, LLC Vol. 1 and Vol. 2, **1996**.

49. Wang, Z.L.; Kang, Z.C. Functional and Smart Materials – Structural Evolution and Structure Analysis; Springer – Verlag, **1998**.

50. Williams, D.B.; Carter, C.B. Transmission Electron Microscopy; Springer Science Business Media, LLC Vol. 4, **1996**.

51. Weber, F.; et. al. *Physica B*; **2005**, *226*, 359 – 361.

52. (a) Smart, J.S. Effective Theories of Magnetism; Saunders: Philadelphia, PA, **1966**. (b) Kittel, C. Introduction to Solid State Physics 7th Ed.; John Wiley and Sons: Hoboken, NJ, **1996**.